

Direct Calculation of Wave Implosion for Detonation Initiation in Pulsed Detonation Engines

Bao Wang¹, Hao He² and S.-T. John Yu³
Ohio State University, Columbus, Ohio, 43202

One- and two-dimensional imploding waves are numerically simulated by using the space-time CESE method. One-dimensional calculations show that a Mach 1.3 converging shock is capable to initiate the detonation in a 2:1:7 H₂/O₂/Ar gas mixture, initially at 0.2 standard atmospheric pressure. Results also clearly show a two-shock implosion system, resulting from interactions between the reflected main shock and the contact discontinuity wave. Implosion of the second shock pushes pressure and temperature at the focal region to be more than 5000 times higher than its initial values. Two-dimensional solutions focus on imploding polygonal shock fronts. Corners of the polygon are the source of complex Mach reflection. In each polygonal section, the flow field is analogous to a planar shock wave entering a channel with converging walls. Numerical images show complex and spectacular shock structure. Similar to that in one-dimensional results, histories of pressures at the focal point also show a multiple-implosion system.

I. Introduction

There has recently been intense interest in pulse detonation engines (PDEs) which generate thrust via a cyclical detonation process. Although it is highly desirable that PDEs use combustible fuels which have already been approved by the aviation industry, the resulting fuel-air mixtures are difficult to detonate. One means of initiating these mixtures is via the use of a “pre-detonator” or “driver” tube which is filled with highly detonable fuel-oxygen. Spark ignition of this mixture leads to a detonation wave which can then be used to initiate the fuel-air mixture in the main combustion chamber. It is desirable from both a safety and performance point of view to keep the volume of the pre-detonator as small as possible. Thus, the efficiency of transmission from the driver tube to the chamber will be an important issue. One means of promoting transmission is shock reflection and focusing techniques.

Murray et al.¹ proposed to transmit detonation waves from an initiator into the main detonation tube through an annular orifice. The diameter of the main tube could be 2.2 times of the diameter of the initiator. The annular orifice generated an imploding toroidal wave and the high-pressure and high-temperature focal region is capable of sustaining detonations in the main chamber.

Recently, Shepherd and coworkers^{2,3} have successfully developed an efficient imploding detonation initiator based on the use of an array of small channels to generate and merge multiple shock waves to create a single toroidal shock front in the main detonation chamber. The collapsing shock front compresses the gas mixture adiabatically as it flows into an ever-decreasing area, leading to a focal region of extremely high energy density. Compressing the gas mixtures increases the post-detonation wave pressure to be higher than the Chapman-Jouguet (CJ) pressure, resulting in an increasingly overdriven detonation wave for detonation transmission from an initiator into the main detonation engine. This shock focusing mechanism depends only on the flow geometry and provides the means to dramatically increase the transmission efficiency and to reduce the required amount of sensitized initiator gas. They showed that by using this technique, detonations were realized in a C₃H₈-air mixture at room temperature (298 K).

To analyze implosion and explosion blast waves, classical self-similar solutions provide useful scaling relationships and greatly facilitate the analyses. In general, a self-similar solution represents an asymptotical flow regime, which is approached by the flow solution after the initial complex flow structure fades away. Based on dimensional analyses, the classical self-similar solution of expanding blast wave was developed by Taylor⁴ and Sedov.⁵ Later the analytical solution was further refined by many researchers, e.g., Sharma and Radha⁶ Toque,⁷ and van Dyke and Guttman.⁸ We note that in this solution, the central region, from where the blast wave emanates, is without any flow structure. This is true when the blast wave has propagated far away from the center and all wave structures in the initiation process have been dissipated.

¹ Graduate student assistant, Mechanical Engineering, wang.909@osu.edu.

² Graduate student assistant, Mechanical Engineering, he.94@osu.edu, AIAA student member.

³ Associate professor, Mechanical Engineering, yu.274@osu.edu, AIAA member.

In a similar method, solution of imploding wave was provided by Guderley.⁹ However, the time and length scales of implosion are much smaller than that of explosion, and there is not enough space and time for an imploding flow to develop and reach its asymptotic state. Thus, the Guderley solution is less useful, unless the imploding blast wave is initiated exactly as the analytical solution.

Other theoretical and experimental studies of imploding and exploding blast waves have been conducted by researchers, e.g., Boyer,¹⁰ Friedman,¹¹ Glass,¹² Baker,¹³ and Schwendeman and Whitham¹⁴. There have been few satisfactory implosion experiments because it is extremely difficult to break a spherical diaphragm instantaneously.

Numerical experiments have also been carried out for implosion and explosion problems. For example, Flores and Holt¹⁵ employed Glimm's scheme to compute the explosion generated by a pressurized sphere in water. Charrier and Tessieras¹⁶ calculated a cylindrical explosion in air by using a front-tracking technique. Oran and DeVore¹⁷ used the FCT method and connection machine to solve two-dimensional imploding detonation waves with and without perturbation. Payne¹⁸ used the Lax method and conducted calculations of converging cylindrical shock. Falcovitz and Birman¹⁹ used the GRP method and studied strong and weak discontinuities in explosion/implosion flows. The GRP method uses a moving mesh to track the discontinuities and a cell-merging-splitting mechanism to avoid small cells that invariably lead to extremely small time steps for numerical stability. The method is rather complex and its extension to multidimensional flows could be difficult. Sod²⁰ proposed an operator splitting method to overcome the singularity problem at the focal center. He solved an implosion problem and showed the existence of the second implosion due to the interactions between the reflected main shock with the incoming contact discontinuity. As will be shown in the present paper, this second implosion shock plays a critical role in detonation initiation processes.

The goal of the present paper is to analyze complex structure of converging shocks. We use the Space-Time Conservation Element and Solution Element (CESE) method²¹⁻²⁴ to solve the one- and two-dimensional reacting Euler equations in cylindrical and Cartesian coordinates, respectively. In one-dimensional simulation, we focus on detonation initiation processes in a H₂/O₂/Ar mixture. Chemical reactions are modeled by a finite-rate chemistry model of 10 species and 24 reaction steps. Numerical results clearly show a triple shock system and complex wave interactions. Apparently, ignition is greatly enhanced by the implosion of the second shock, owing to the interaction between the outwardly moving reflected main shock and the inwardly moving contact discontinuity.

In two-dimensional calculations, we consider both reacting flow and non-reacting flows. For reacting flows, a global reaction model is adopted to model C₃H₈-air combustion for numerical efficiency. Circular imploding flows with small perturbations on the shock front as well as polygonal shock fronts are considered. In order to study complex flow features, we use up to 4.5 million mesh nodes to calculate the imploding flows. The calculation was performed by using a newly constructed 32-node Beowulf cluster at OSU. In the imploding phase of the flow, the CESE method is able to maintain the cylindrical symmetry of the implosion waves and track the main features of the flow near the focal point of the incoming waves. Among its many merits, the CESE method is a genuinely un-split numerical method, and it can provide highly accurate solutions of complex curved shocks. Although much remains to be done to address the abovementioned numerical issues, we visibly demonstrate in the present paper that the CESE method does not suffer significant deficiency in calculating the implosion solutions.

The rest of the present paper is organized as follows. Section 2 gives governing equations. Section 3 presents and validates numerical method employed. Section 4 discusses the one-dimensional numerical results. Section 5 discusses the two-dimensional implosion results. We then provide the concluding remarks, acknowledge helps that we received during the course of the present work, and provide the list of cited references.

II. Governing equations

The governing equations for the numerical simulation are the one-dimensional multi-species reactive Euler equations of N_s species:

$$\frac{\partial \mathbf{U}}{\partial t} + \frac{\partial \mathbf{F}(\mathbf{U})}{\partial r} = \mathbf{G}(\mathbf{U}) + \mathbf{S}(\mathbf{U}) \quad (2.1)$$

where

$$\begin{aligned} \mathbf{U} &= (\rho, \rho u, \rho E, \rho_1, \rho_2, \dots, \rho_{N_s-1})^T \\ \mathbf{F} &= (\rho u, \rho u^2 + p, (\rho E + p)u, \rho_1 u, \rho_2 u, \dots, \rho_{N_s-1} u)^T \\ \mathbf{G} &= -\frac{j}{r} (\rho u, \rho u^2, (\rho E + p)u, \rho_1 u, \rho_2 u, \dots, \rho_{N_s-1} u)^T \\ \mathbf{S} &= (0, 0, 0, \dot{\omega}_1, \dot{\omega}_2, \dots, \dot{\omega}_{N_s-1})^T \end{aligned} \quad (2.2)$$

where ρ , u , p , E , and ρ_k are density, velocity, specific total energy, and mass concentration of species k , respectively. $j = 0, 1, 2$ for planar, cylindrical, and spherical flows, respectively. ρ is the summation of all species density,

$$\rho = \sum_{k=1}^{N_s} \rho_k \quad (2.3)$$

The total energy E is defined as

$$E = e + u^2 / 2 \quad (2.4)$$

where e is the internal energy of the gas mixture per unit mass and it is calculated based on a mass-weighted average of the specific internal energy of each species e_k , i.e.,

$$e = \sum_{k=1}^{N_s} y_k e_k \quad (2.5)$$

In Eq. (2.5), $y_k = \rho_k / \rho$ is the mass fraction of species k . Note that since the internal energy e and the total energy E include the heat of formation of each species in their definitions, no source term exists in the energy equation. $\dot{\omega}_k$ is the net molar production rate of species k and can also be expressed as $\dot{\omega}_k = \rho \Omega_k / W_k$.

According to the law of mass action, the stoichiometric equation of a set of N_r elementary reactions involving N_s species can be written in the following form

$$\sum_{k=1}^{N_s} \nu'_{jk} n_k \xrightleftharpoons[K_{bj}]{K_{fj}} \sum_{k=1}^{N_s} \nu''_{jk} n_k, \quad j = 1, 2, \dots, N_r \quad (2.6)$$

where $n_k = \rho_k / W_k$ is the mole concentration of species k in the gas mixture. ν'_{jk} and ν''_{jk} are respectively the stoichiometric coefficients of the reactants and products of species k in the j th reaction. The source terms, $\dot{\omega}_k$ for $k=1, 2, 3, \dots, N_s-1$, in the species equations, Eq. (2.2), are formulated in mass concentration, and they are the summation of the net rate of change of species k from all chemical reactions involved, i.e.,

$$\dot{\omega}_k = W_k \sum_{j=1}^{N_r} (\dot{n}_k)_j \quad (2.7)$$

where W_k is the molecular weight of species and $(\dot{n}_k)_j$ is the rate change of concentration of species k by the reaction j , given by

$$(\dot{n}_k)_j = (\nu''_{jk} - \nu'_{jk}) \left(K_{fj} \prod_{l=1}^{N_s} n_l^{\nu'_{lj}} - K_{bj} \prod_{l=1}^{N_s} n_l^{\nu''_{lj}} \right) \quad (2.8)$$

The forward and backward reaction rate constants, K_{fj} and K_{bj} , are in the Arrhenius form:

$$\begin{aligned} K_{fj} &= A_{fj} T^{B_{fj}} \exp(-E_{fj} / R_u T) \\ K_{bj} &= A_{bj} T^{B_{bj}} \exp(-E_{bj} / R_u T) \end{aligned} \quad (2.9)$$

where A_f and A_b are the pre-exponential constant; E_f and E_b are the activation energies; and R_u is the universal gas constant. In general, those coefficients in Eq. (2.9) are provided as a part of the adopted finite-rate chemistry model. If the kinetic data of the reverse reaction were not available, one needs to use the equilibrium constant to calculate the reverse reaction rate constants, i.e.,

$$K_{bj} = K_{fj} / K_{eqj} \quad (2.10)$$

where the K_{eqj} is determined by minimizing the free energy.²⁵

III. Numerical method

The space-time Conservation Element Solution Element (CESE) method, originally proposed by Chang²¹ has been extended for chemical reacting flows with realistic finite-rate chemistry models. The CESE method is distinguished by the simplicity of its design principle, i.e., treating space and time as one entity in calculating flux conservation. Previously, we have reported the extension of the CESE method for chemically reacting flows with comprehensive physical modeling, including the multi-step finite-rate kinetics and thermodynamics models.^{26,27}

The details of the Space-Time CE/SE method have been extensively illustrated in the cited references. For completeness, only a brief discussion of the essential steps of the CE/SE method will be provided here. We shall first discuss the conventional finite-volume methods, in which because space and time are not treated equally, the choice of

the space-time geometry has been restricted. As discovered by Godunov, the classical Riemann problem was encountered in balancing the space-time flux. Thus a Riemann solver became an integral part of the modern upwind schemes. In the present space-time CE/SE method, however, due to an equal footing treatment of space and time, the resultant formula is flexible to allow a better choice of space-time geometry to calculate flux conservation. In particular, a zigzagging strategy was developed such that the Riemann problem was avoided in balancing the space-time flux. Moreover, the spatial gradients of the flow variables are also treated as the unknowns and they march in time hand in hand with the flow variables themselves. As a result, no Riemann solver or reconstruction step is used as the building block. The logic of the present method is much simpler. In the following subsections, we shall illustrate the basic concept of the space-time integration in the CE/SE method as a contrast to the conventional methods. We then illustrate the essential steps of the present method in calculating the detonations.

A. Conventional Finite-Volume Methods

The conventional finite-volume methods for solving conservation laws were formulated according to flux balance over a *fixed spatial domain*. The conservation laws state that the rate of change of the total amount of a substance contained in a fixed spatial domain V is equal to the flux of that substance across the boundary of V , i.e., $S(V)$. Let the density of the substance be u and its spatial flux be f , the convection equation can be written as

$$\frac{\partial u}{\partial t} + \frac{\partial f}{\partial x} = \tau(u) \quad (3.1)$$

where $\tau(u)$ is the source term in the convection equation. According to the Reynolds transport theorem, the integral form of the above equation can be expressed as:

$$\frac{\partial}{\partial t} \int_V u dV = - \int_{S(V)} f \cdot d\vec{s} + \int_V \tau(u) dV \quad (3.2)$$

The conventional finite-volume methods concentrated on calculating the surface flux, i.e., the first term on the right hand side. The time derivative term is usually treated by a finite difference method, e.g., the Runge-Kutta method. Or, integration can be performed for temporal evolution:

$$\int_V u dV \Big|_{t_1}^{t_2} = \int_{t_1}^{t_2} \left(- \int_{S(V)} f \cdot d\vec{s} + \int_V \tau(u) dV \right) dt \quad (3.3)$$

Due to the *fixed spatial domain*, the shape of the space-time Conservation Elements (CEs) in one spatial dimension for Eq. (3.3) must be rectangular. Refer to Fig. 3.1(a). The unknowns are usually placed at the center of the spatial mesh, i.e., on the boundary of the space-time CEs. The CEs must stack up exactly on the top of each other in the temporal direction, i.e., no staggering of these elements in time is allowed. For equations in two space dimensions, as depicted in Fig. 3.1(b), a conservation element is a uniform-cross-section cylinder in the space-time domain, and again no staggering in time is allowed.

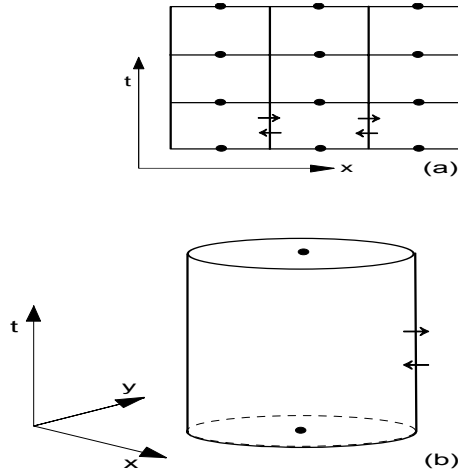


Figure 3.1 Space-time integration for conventional finite-volume methods in one and two spatial dimensions.

This arrangement results in vertical interfaces extended in the direction of time evolution between adjacent space-time conservation elements. Across these interfaces, flow information travels in both directions. Therefore, an upwind bias method (or a Riemann solver) must be employed to calculate the interfacial fluxes.

B. The Space-Time Integration

Consider an initial-value problem involving the PDE,

$$\frac{\partial u}{\partial t} + a \frac{\partial u}{\partial x} = \tau(u) \quad (3.4)$$

where a is a constant and $\tau(u)$ is a function of u . Let $x_1 = x$ and $x_2 = t$, be the coordinates of a two-dimensional Euclidean space E_2 . Thus Eq. (3.4) becomes a divergence free condition,

$$\nabla \cdot \mathbf{h} = \tau(u) \quad (3.5)$$

where the current density vector $\mathbf{h} = (au, u)$. By using Gauss' divergence theorem in the space-time E_2 , it can be shown that Eq. (3.4) is the differential form of the integral conservation law:

$$\oint_{S(R)} \mathbf{h} \cdot d\mathbf{s} = \int_R \tau(u) dR \quad (3.6)$$

Figure 3.2 is a schematic for Eq. (3.6).

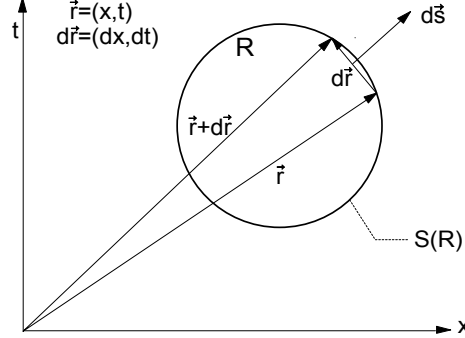


Figure 3.2 A schematic of the space-time integral.

Here $S(R)$ is the boundary of an arbitrary space-time region R in E_2 , $d\mathbf{s} = d\sigma \bar{\mathbf{n}}$ with $d\sigma$ and $\bar{\mathbf{n}}$, respectively, being the area and the outward unit normal of a surface element on $S(R)$, and dR is the volume of a space-time region inside $S(R)$. Note that $\mathbf{h} \cdot d\mathbf{s}$ is the space-time flux of \mathbf{h} leaving the region R through the surface element $d\mathbf{s}$, and all mathematical operations can be carried out since E_2 was an ordinary two-dimensional Euclidean space. We remark that space and time are treated on an equal footing manner. Therefore, there is no restriction on the space-time geometry of the conservation elements over which the space-time flux is imposed.

Let Ω denote the set of all staggered space-time mesh nodes (j, n) in E_2 (dots in Fig. 3.3(a)) with n being a half or whole integer, and $(j - n)$ being a half integer. For each $(j, n) \in \Omega$, let the solution element $SE(j, n)$ be the interior of the space-time region bounded by a dashed curve depicted in Fig. 3.3(b). It includes a horizontal line segment, a vertical line segment, and their immediate neighborhood. For the discussions given in this paper, the exact size of this neighborhood does not matter.

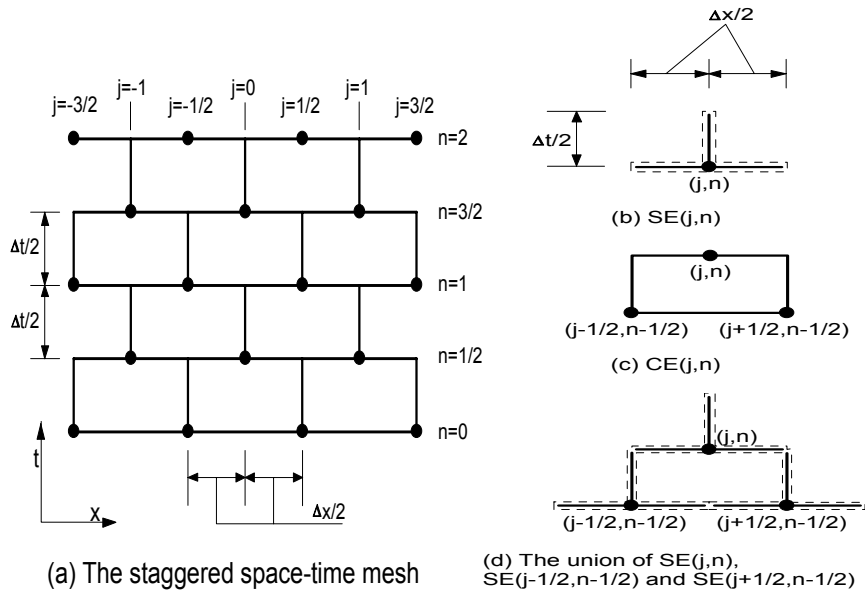


Figure 3.3 The space-time mesh of the CE/SE method.

For any $(x, t) \in \text{SE}(j, n)$, let $u(x, t)$ and $\mathbf{h}(x, t)$, respectively, be approximated by $u^*(x, t; j, n)$ and $\mathbf{h}^*(x, t; j, n)$ which we shall define shortly.

Let

$$u^*(x, t; j, n) = u_j^n + (u_x)_j^n(x - x_j) + (u_t)_j^n(t - t^n) \quad (3.7)$$

where (i) u_j^n , $(u_x)_j^n$ and $(u_t)_j^n$ are constants in $\text{SE}(j, n)$, and (ii) (x_j, t^n) are the coordinates of the mesh point (j, n) . As will be explained later, we shall assume that

$$(u_t)_j^n = -a(u_x)_j^n \quad (3.8)$$

Combining Eqs. (3.7) and (3.8), one has

$$u^*(x, t; j, n) = u_j^n + (u_x)_j^n[(x - x_j) - a(t - t^n)], \quad (3.9)$$

$$(x, t) \in \text{SE}(j, n)$$

As a result, there are two independent marching variables u_j^n and $(u_x)_j^n$ associated with each $(j, n) \in \Omega$. Furthermore, because $\mathbf{h} = (au, u)$, we define

$$\mathbf{h}^*(x, t; j, n) = (au^*(x, t; j, n), u^*(x, t; j, n)) \quad (3.10)$$

Let E_2 be divided into non-overlapping rectangular regions referred to as conservation elements (CEs). As depicted in Fig. 3.3(c), the CE with the midpoint of its top face being any mesh point $(j, n) \in \Omega$ is denoted by $\text{CE}(j, n)$. The discrete approximation of Eq. (3.6) is

$$\oint_{S(\text{CE}(j,n))} \mathbf{h} \cdot d\mathbf{s} = \tau(u_j^n) \times \frac{\Delta x \Delta t}{2} \quad (3.11)$$

Here $\tau(u_j^n)$ is assumed to be the average value of $\tau(u)$ in $\text{CE}(j, n)$. Because $(\Delta x \Delta t)/2$ is the volume of $\text{CE}(j, n)$, Eq. (3.11) simply states that the total space-time flux of \mathbf{h}^* leaving the boundary of any CE is equal to the source integral over the CE. Because the surface integration over any interface separating two neighboring CEs is evaluated using the information from a single SE, obviously the local conservation relation Eq. (3.11) leads to a global flux conservation relation, i.e., the total flux of \mathbf{h}^* leaving the boundary of any space-time region that is the union of any combination of CEs is equal to the source integral over the same space-time region.

To justify Eq. (3.8), we shall assume that the value of u on a macro scale (that is the value of u obtained from an averaging process involving a few neighboring CEs) will not vary significantly as a result of redistribution of τ over each CE, in which τ is held constant. Based on this assumption, we take the liberty to redistribute the source term such that there is no source present within each SE. Thus with the aid of Eq. (3.7), Eq. (3.8) is the result of substituting $u = u^*(x, t; j, n)$ into Eq. (3.6).

Because the boundary of $\text{CE}(j, n)$ is a subset of the union of $\text{SE}(j, n)$, $\text{SE}(j-1/2, n-1/2)$ (refer to Fig. 3.3(d)), Eqs. (3.9-11) imply that

$$u_j^n - \frac{\Delta t}{2} \tau(u_j^n) = \frac{1}{2} [(1 - \nu) u_{j+1/2}^{n-1/2} - (1 - \nu^2)(u_x^+)_{j+1/2}^{n-1/2} + (1 + \nu) u_{j-1/2}^{n-1/2} + (1 - \nu^2)(u_x^+)_{j-1/2}^{n-1/2}] \quad (3.12)$$

Here, (i) $\nu \equiv (a \Delta t) / \Delta x$ is the Courant number and (ii) $(u_x^+)_{j \pm 1/2}^n \equiv (\Delta x / 4) (u_x)_j^n$, $(j, n) \in \Omega$, is the normalized form of $(u_x)_j^n$. Given the values of the marching variables at the $(n - 1/2)$ th time level, u_j^n is determined by solving Eq. (3.12) with the aid of Newton's iteration method. Note that, in the solver of the ZND wave, the initial estimated solution for Newton's iterations is calculated by assuming that the source term is zero. After u_j^n is known, $(u_x^+)_{j \pm 1/2}^n$ is evaluated using an oscillation-suppressing procedure, which was described fully in [22,23]. Here, only a brief account is provided. Let $(j, n) \in \Omega$. With the aid of Eq. (3.8), we have

$$\begin{aligned} u_{j \pm 1/2}^n &\equiv u_{j \pm 1/2}^{n-1/2} + \frac{\Delta t}{2} (u_t)_{j \pm 1/2}^{n-1/2} \\ &\equiv u_{j \pm 1/2}^{n-1/2} - 2\nu (u_x^+)_{j \pm 1/2}^{n-1/2} \end{aligned} \quad (3.13)$$

According to Eq. (3.13), $u_{j \pm 1/2}^n$ can be interpreted as a first-order Taylor's approximation of u at $(j \pm 1/2, n)$. Let

$$\begin{aligned} (u_x^+)_{j \pm 1/2}^n &\equiv \pm (u_{j \pm 1/2}^n - u_j^n) \\ &= \pm \frac{\Delta x}{4} \frac{u_{j \pm 1/2}^n - u_j^n}{\Delta x / 2} \end{aligned} \quad (3.14)$$

where $(u_{x+}^+)_{j \pm 1/2}^n$ and $(u_{x-}^+)_{j \pm 1/2}^n$, aside from a normalized factor $\Delta x/4$, are two numerical analogues of $\partial u / \partial x$ at (j, n) with one being evaluated from the right and the other evaluated from the left. Let the function W be defined by (i) $W(0, 0, \alpha) = 0$ and (ii)

$$W(x_-, x_+, \alpha) = \frac{|x_+|^\alpha x_- + |x_-|^\alpha x_+}{|x_+|^\alpha + |x_-|^\alpha} \quad (3.15)$$

Then $(u_x^+)_j^n$ is calculated using

$$(u_x^+)_j^n = W((u_{x^+})_j^n, (u_{x^-})_j^n, \alpha) \quad (3.16)$$

By using the procedures described,²⁸ the above scheme can be easily extended to become the solver of a nonlinear conservation equations with stiff source terms in either one-dimensional or multidimensional space. In addition to the present work, other CE/SE work related to the 1D and 2D problems with stiff source terms are also studied.²⁹

For validation, cylindrical explosion³⁰ is calculated and the results are compared with the one-dimensional radial RCM solution at time $t=0.25$. The initial condition is given as below

$$\begin{cases} P_{in} = 1.0 \\ \rho_{in} = 1.0 \\ u_{in} = 0.0 \end{cases}, \text{ and } \begin{cases} P_{out} = 0.1 \\ \rho_{out} = 0.125 \\ u_{out} = 0.0 \end{cases} \quad (3.17)$$

The snapshots agree very well with the results got by RCM method, as shown in Fig. 3.4.

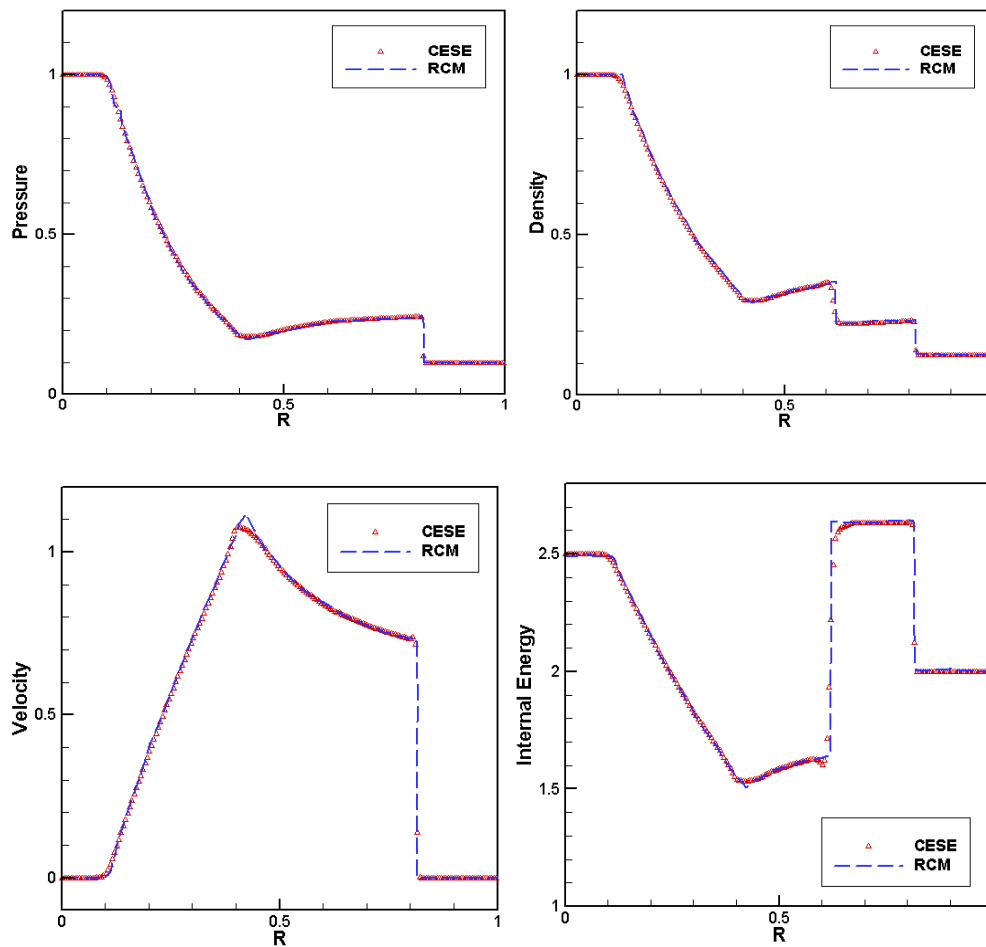


Figure 3.4 CESE results compared with RCM solution

Another example is the repeat of Sedov's solution.⁵ First, Sedov's solution at time $t=2.8e-6$ is taken as input, then the results after $\Delta t = 1.92e-8$ are compared with Sedov's solution, shown in Fig 3.4.

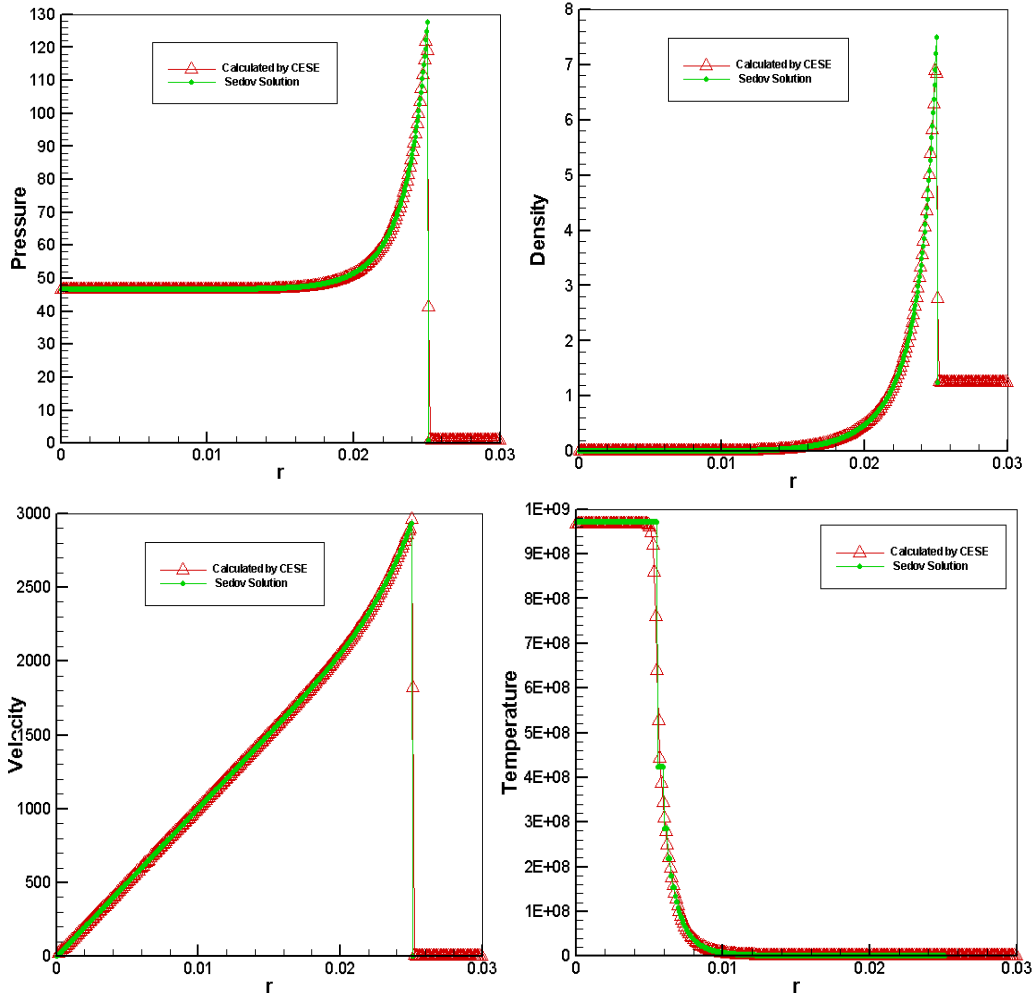


Figure 3.4 CESE results compared with Sedov's solution

IV. One-Dimensional Implosion

In a one-dimensional cylindrical coordinate system, the initial conditions are composed of two regions, separated at $r = r_o$. In all results, $r_o = 0.1$ meter, and the computational domain is $0 < r < 0.38$ meter. 14,400 equally spaced mesh nodes are used to cover the whole spatial domain. To maintain numerical stability, the time step size is dynamically adjusted, and, in general, $0.5 < CFL < 0.8$. In the driving region, where $r > r_o$, we consider two initial pressures: 10 atm and 1 atm. In the driven region, where $r < r_o$, the initial pressure is 0.2 atm. In all calculations, the initial temperature of the whole domain is 300 K and mole concentration ratio of the $H_2/O_2/Ar$ gas mixture is 2:1:7. Note that most of the results presented in the paper is for the case of $P_{out}/P_{in} = 50$. For $P_{out}/P_{in} = 5$, only limited results are presented and compared with the $P_{out}/P_{in} = 50$ case.

We start the computation when the diaphragm separating the two flow regions is suddenly released. Figures 4.1, 4.2 and 4.3 show the snapshots of pressure, density, and velocity profiles at various times. Note that values of the flow variables in the implosion phase of the flow problem are significantly different from that of the exploding phase. Thus, two plots are provided for each flow variables. Figures 4.4 shows detailed space-time flow patterns of pressure, density, temperature, velocity. Figure 4.5 shows mass fraction of the radical species OH.

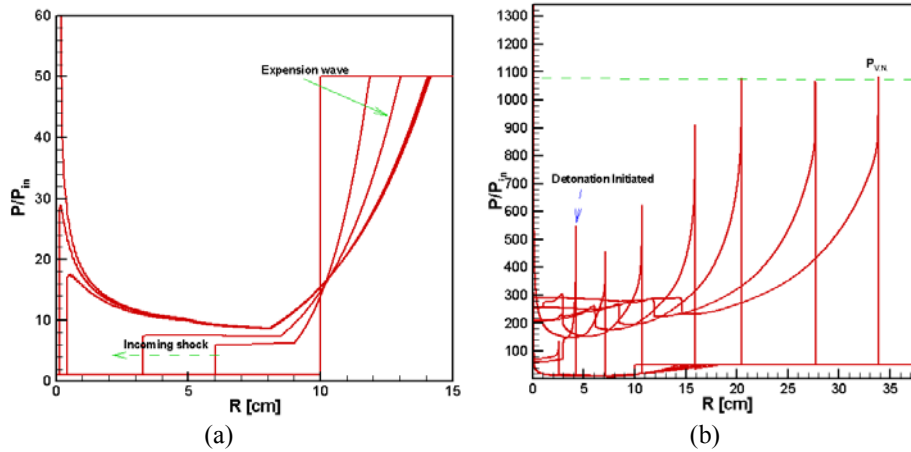


Figure 4.1 Pressure profiles at various times for $P_{out}/P_{in}=50$. (a) Implosion. (b) Explosion

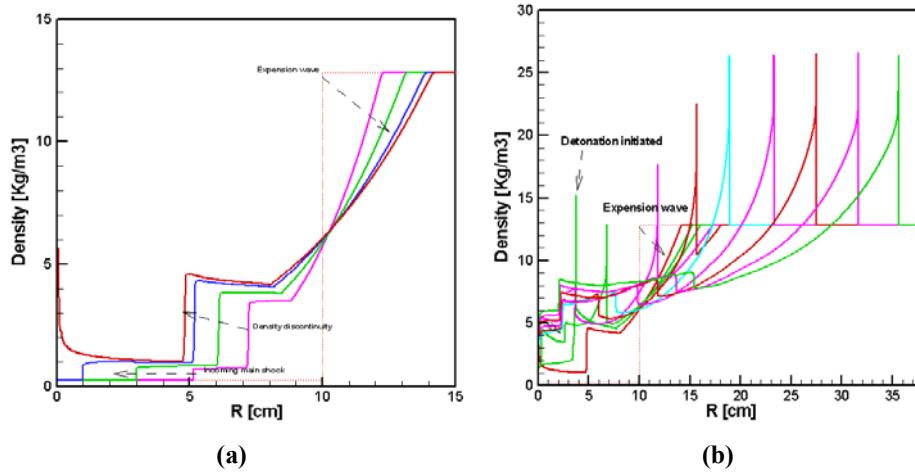


Figure 4.2 Density profiles at various times for $P_{out}/P_{in}=50$. (a) Implosion. (b) Explosion.

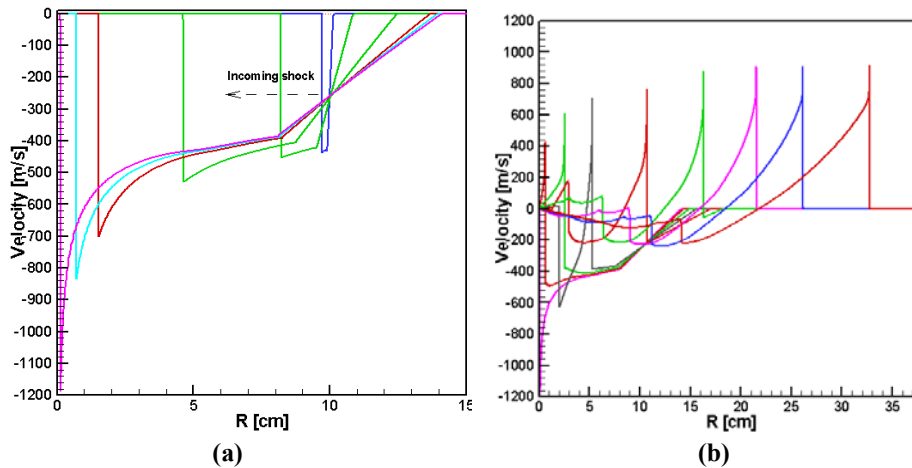


Figure 4.3 Velocity profiles at various times for $P_{out}/P_{in}=50$. (a) Implosion. (b) Explosion.

The initial flow development is similar to that of Sod's shock-tube problem. Owing to the initial pressure difference, a shock wave is generated and it moves inwardly towards the axis. A rarefaction wave moves outwardly away from the axis. Between the rarefaction wave and the shock, a contact discontinuity appears and it moves towards the axis.

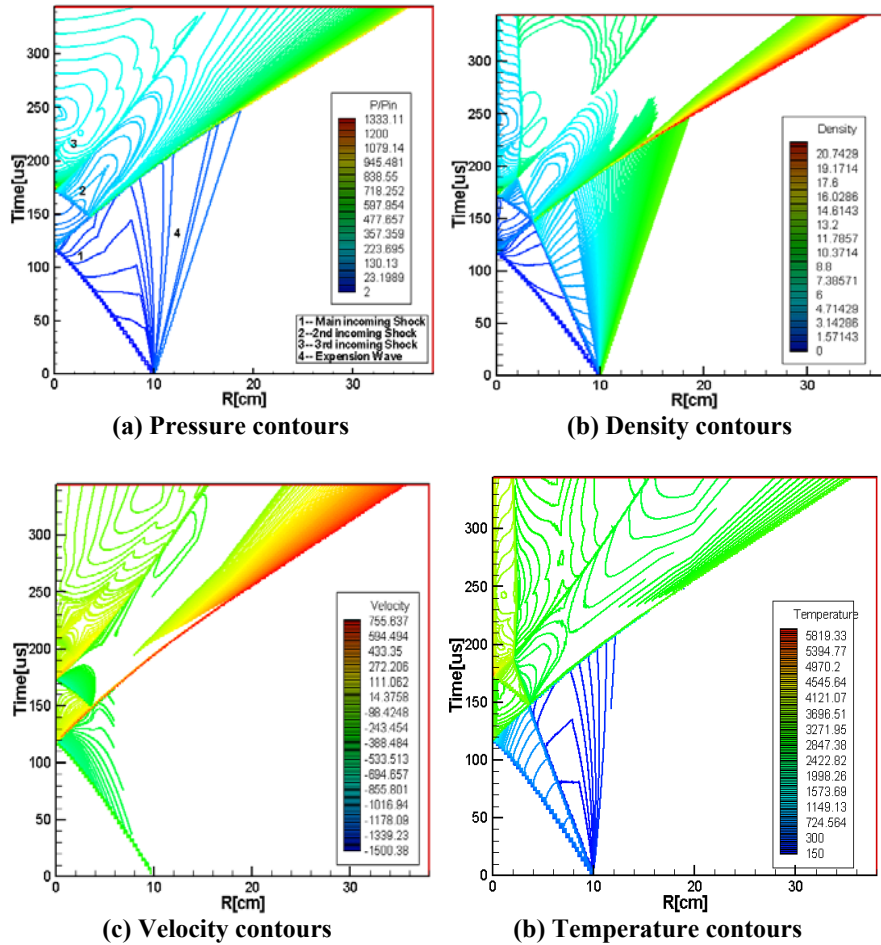


Figure 4.4 Flow variables contours in the computational space-time domain for $P_{out}/P_{in} = 50$.

Due to ever-decreasing area, both pressure and velocity immediately behind the main shock steadily increases as time progresses. After its reflection from the axis and moves outwardly, the main shock clashes with the incoming contact discontinuity. Afterwards, the main shock penetrates the contact discontinuity and moves outwardly with a constant speed. The interaction causes the contact discontinuity to slightly slow down in its inward motion. Simultaneously, a new shock is generated at the point of interaction and it moves quickly towards the axis. Implosion of this second shock raises the pressure and temperature at the focal point even higher. This double implosion mechanism is the main mechanism for initiating the detonation at the focal region. In the explosion phase of the flow, a robust detonation could be clearly discerned for $r > 10$ cm in Figs. 4.1-4.4.

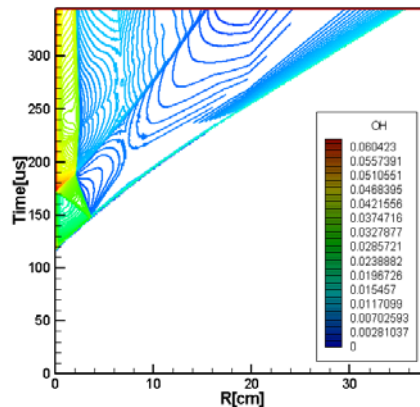


Figure 4.5 OH contour for $P_{out}/P_{in}=50$ in the computational space-time domain.

Similar to that of the main shock, the reflected second shock interacts with the contact discontinuity and generates a third imploding shock, which is weak and cannot be easily discerned in Figs. 4.1-4.4. After interacting with the reflected second shock, the contact discontinuity stops its inward motion and become stationary at $r = 2$ cm. This stationary contact discontinuity could be seen as a vertical line along $r = 2$ cm in Figs. 4.4-4.5.

Figures 4.6-4.9 show the comparison of the flow conditions between the case of $P_{out}/P_{in} = 50$ and the $P_{out}/P_{in} = 5$ case. Figure 4.6 shows the space-time trajectories of the main shocks. Near the focal point, imploding shocks and exploding shocks of both cases deviate from a straight line. While the trajectory slopes of imploding shocks in two cases are markedly different due to the different shock strengths, the exploding shocks have nearly identical slopes because in both cases detonations have been successfully initiated. Away from the focal region, $r > 10$ cm, robust detonations propagate at the CJ velocity can clearly seen in Figs. 4.4.

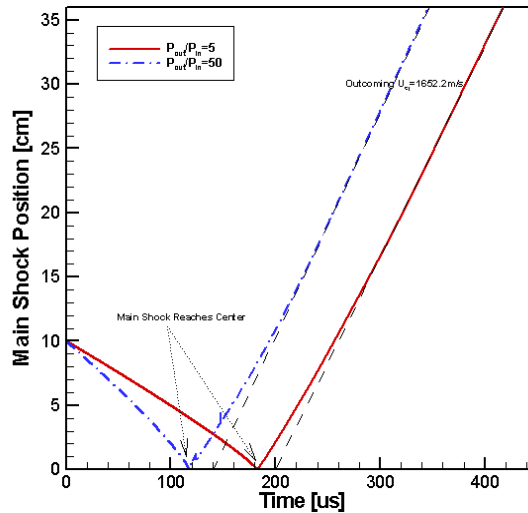


Figure 4.6 Space-time trajectories of the main shocks of the $P_{out}/P_{in}=5$ and $P_{out}/P_{in}=50$ cases.

Figure 4.7-9 shows the time histories of pressure, density, and temperature at the focal point of implosion. For the case of $P_{out}/P_{in} = 50$, one could clearly see the presence of the above- mentioned third shock wave. For the $P_{out}/P_{in} = 5$ case, the third shock is too weak to be detected. The maxima of flow variables were achieved by the implosion of the second shock.

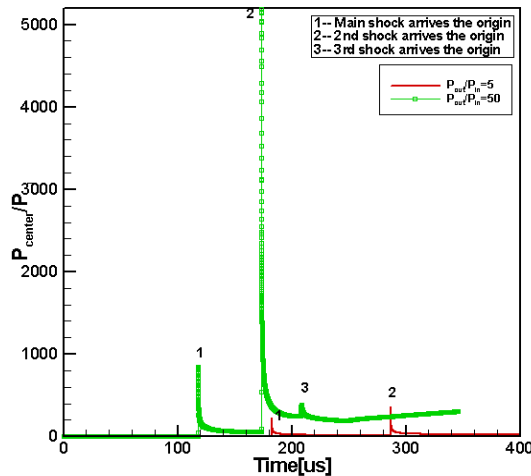


Figure 4.7 Time histories of pressures at the focal point for $P_{out}/P_{in}=5$ and $P_{out}/P_{in}=50$.

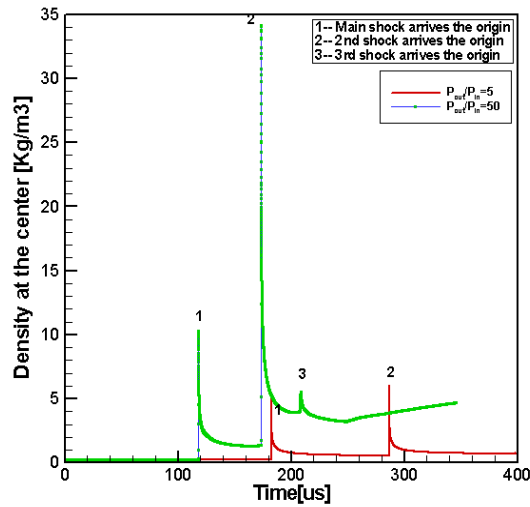


Figure 4.8 Time histories of densities at the focal point for $P_{out}/P_{in}=5$ and $P_{out}/P_{in}=50$.

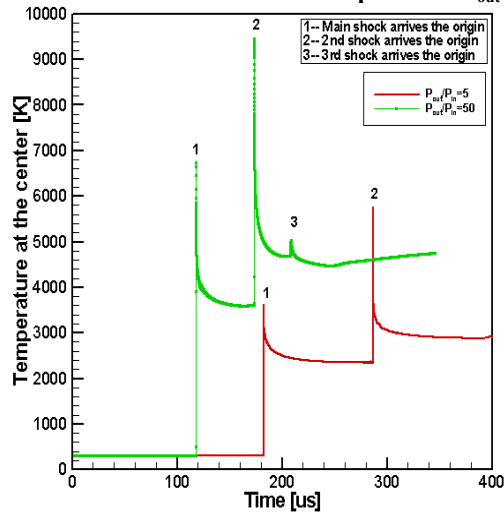


Figure 4.9 Time histories of temperatures at the focal point for $P_{out}/P_{in}=5$ and $P_{out}/P_{in}=50$.

Fig. 4.10 shows trajectory of converging cylindrical shock wave for $Ms=2.1$ ($P_{out}/P_{in} = 50$). It can be clearly seen from the picture that the following relation is valid except near the center

$$\frac{R}{R_c} = \left(1 - \frac{t}{t_c}\right)^\alpha$$

(4.1)

Where R_c is the radius of the starting converging shock and t_c is the time when the converging shock arrives the center. The gradient of the trajectory is obviously the similarity exponent α of Eq. (4.1) in its valid range. In our calculation, for $Ms=2.1$, $\alpha = 0.835$.

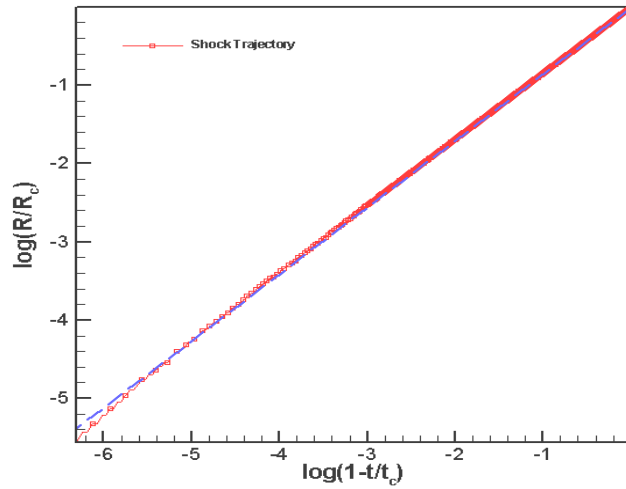


Figure 4.10 Shock trajectory for Ms=2.1.

Previous results are listed in Table A for comparison.

Table A. Previous results of Self-similar exponent

Self-Similar Exponent α	
Guderley (1942)	0.834
Butler (1954)	0.835217
Sanyukovich (1960)	0.834
De Neef and Nechman (1978)	0.835 ± 0.003
Takayama (1984)	0.831 ± 0.002 Ms=1.1-2.1
Kleine (1985)	$0.832^{+0.028}$ Ms=1.3-2.1 -0.043

V. Two-Dimensional Implosion

All calculations use the same unstructured mesh of about 4.5 million quadrilaterals. Figure 5.1 is a schematic of the mesh. Due to symmetry, the actual computational domain is a quarter of the shown circle. The dimensionless radius of the computational domain is 1.0. Four implosion cases are presented here. Three of them are non-reacting implosion with a square front, an octagonal front, and a circular front with sinusoidal perturbations on the shock front. Pressure is perturbed and the amplitude of the perturbation is 2% of the initial pressure difference between the driver section and driven section. There are 32 cycles of sinusoidal perturbations around the whole circular front.

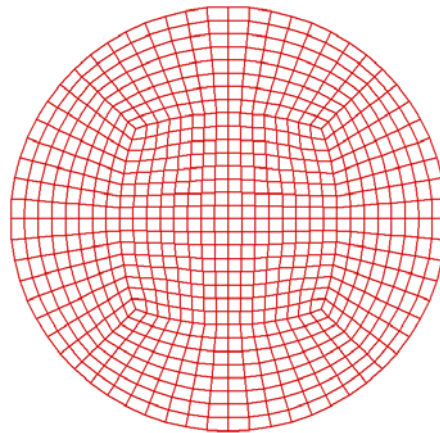


Figure 5.1 A schematic of the mesh.

The fourth implosion case is a reacting circular shock front with similar perturbations. The initial condition is composed of two distinct regions with different pressures. In all calculations here, $P_{out}/P_{in} = 20$ and temperature is uniform at 300 K. Thus, in all cases, $\rho_{out}/\rho_{in} = 20$.

The calculations were performed by using a parallelized CESE Euler solver, running on 27 nodes of a 32-node PC cluster. The simulation ends when the main shock exits the outer boundary of the computational domain. Typical run time of one calculation is about 4 hours on a wall clock. The full capacity of our cluster could handle a mesh about 8 times bigger than the present mesh.

Figures 5.2-5.5 show snapshots of pressure contours at various time steps for the abovementioned four cases. In each case of polygonal shock, flow evolution is symmetric with respect to the bisector of each vertex of the polygon. Imploding shocks interact with the bisector and form Mach reflection. A planar side shock of the polygon corresponds to an incident shock in a shock-on-wedge problem, and the bisector itself corresponds to a wedge surface. Mach reflections can be observed on the bisector from each vertex of the initial polygon. Evolution of each side of a polygonal shock front may be interpreted as a planar shock entering into a convergent shock tube, i.e., a region surrounded by the bisector and the abovementioned lines of symmetry, forming a wedge-shaped cavity.

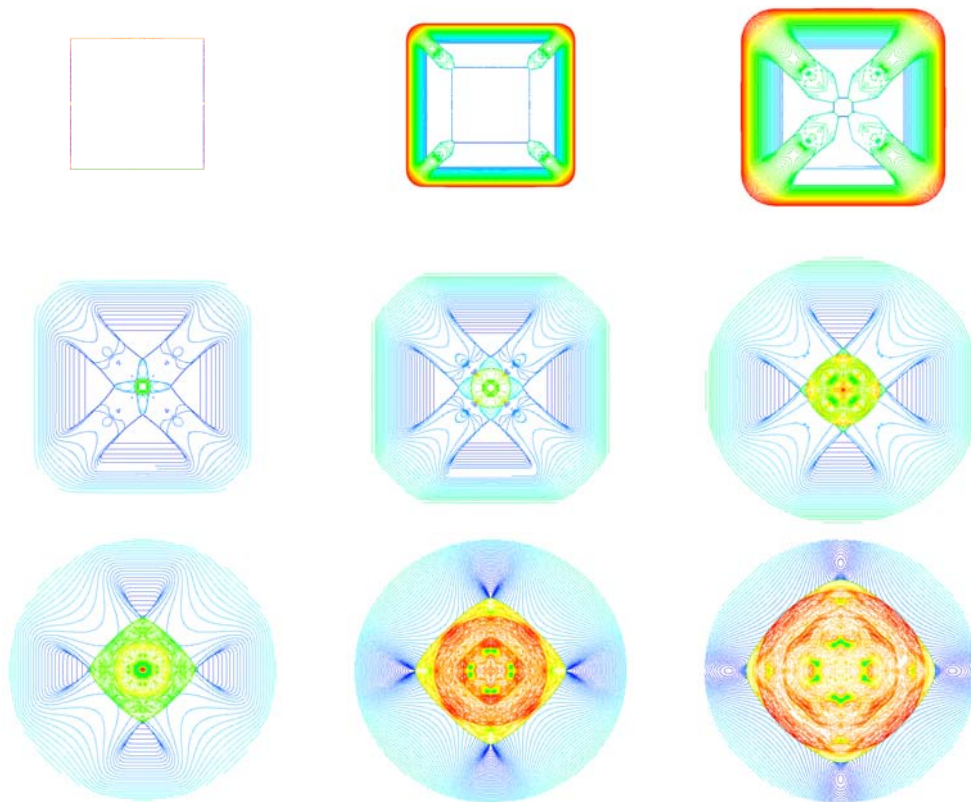


Figure 5.2 Snapshots of pressure contours of a square implosion front at time = 0, 0.1, 0.2, 0.25, 0.3, 0.4, 0.5, 0.65, and 0.8.

In the imploding process, the Mach stem of the Mach reflection propagates with a wave speed faster than that of the initial side shock of the polygonal front. As a result, the Mach stem increases in size, while the length of the side shock decreases to zero. During this evolution, the number of the vertices of the imploding polygon doubles that of the initial polygon. Finally, a new polygon is formed with a similar shape but the orientation is rotated. Seemingly, the original polygon, with a shrunk area, was recovered with a rotated orientation. The sides of this smaller polygon are composed of Mach stems. However, it is known that Mach stems are curved, particularly for weak incident shocks. Thus, the regenerated polygonal shocks have curved sides. One may have multiple regenerations of the initial polygon during the imploding process. This implosion mechanism is markedly different from a cylindrically imploding shock with a smoothly curved surface.

Figure 5.5 shows time histories of temperature and pressure at the focal region for three non-reacting cases. The case of square front has lower pressure and temperature because strong Mach reflections of large incident angles.

For the octagonal and circular fronts, the maximum pressure and temperature are comparable. Perhaps, one could use an octagonal front for effective implosion instead of striving for a circular converging front. Figure 5.5 also shows the second implosion similar to that in the one-dimensional results. Here, no chemical reaction occurs and the second shock is much weaker.

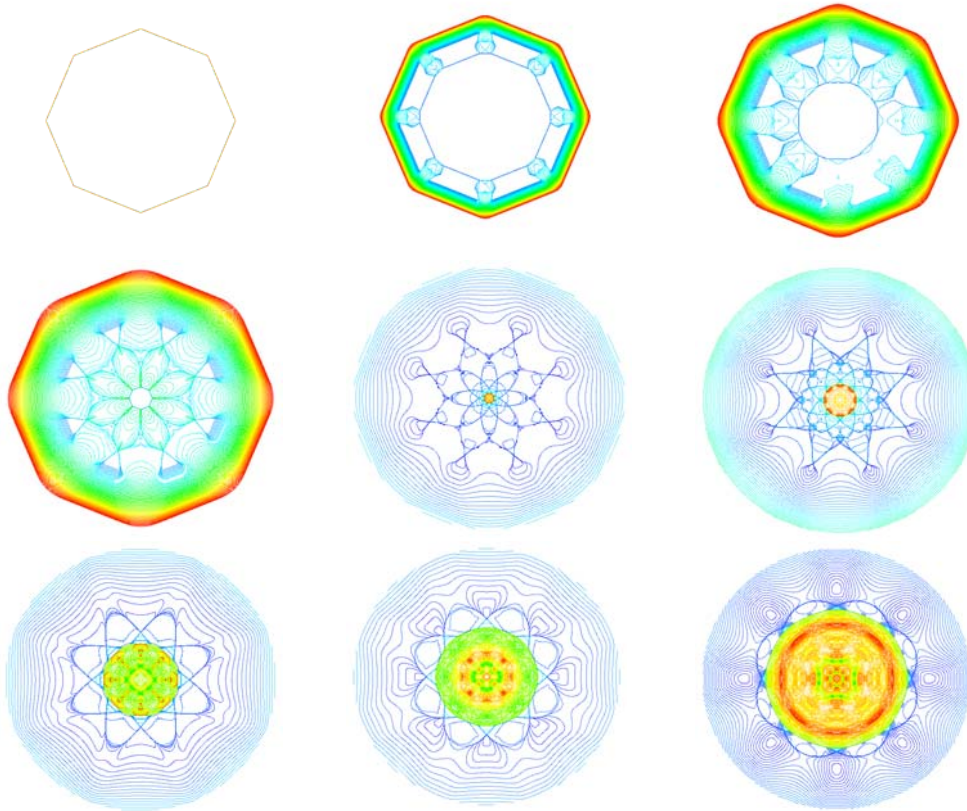
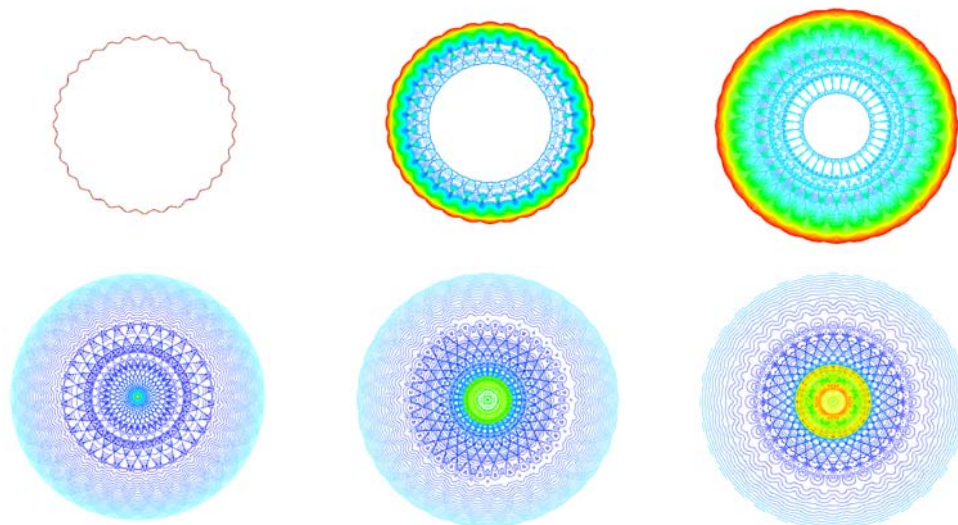


Figure 5.3 Snapshots of pressure contours of an octagonal front at time = 0, 0.09, 0.18, 0.27, 0.315, 0.36, 0.495, 0.63, and 0.72.



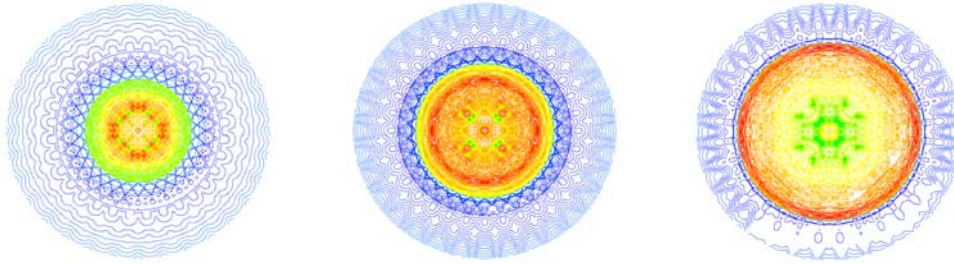


Figure 5.4 Snapshots of pressure contours at time = 0, 0.09, 0.18, 0.27, 0.36, 0.45, 0.585, 0.72, 0.90, respectively.

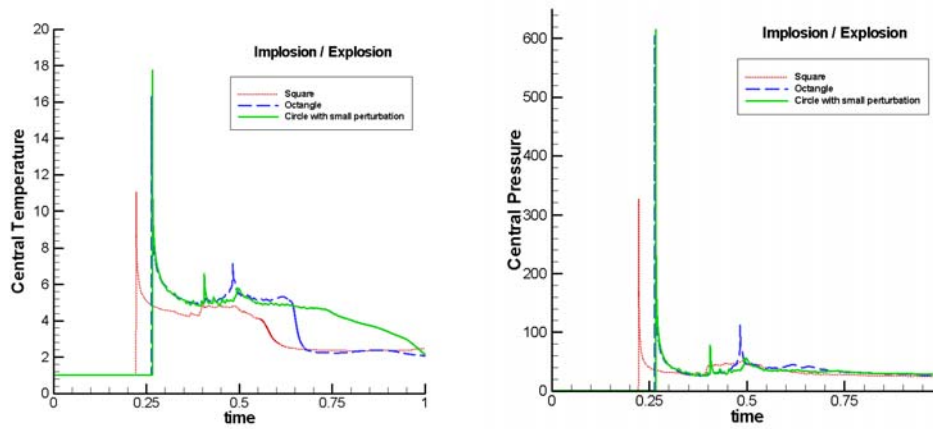


Figure 5.5 Time histories of temperature and pressure at the focal point for the three non-reacting cases.

Figure 5.6 shows the histories of pressure and temperature at the focal point of a successful detonation initiation processes by imploding circular shock front with perturbations on the initial front surface. Similar to the one-dimensional results, consecutive shock implosions with a very strong second shock is evident.

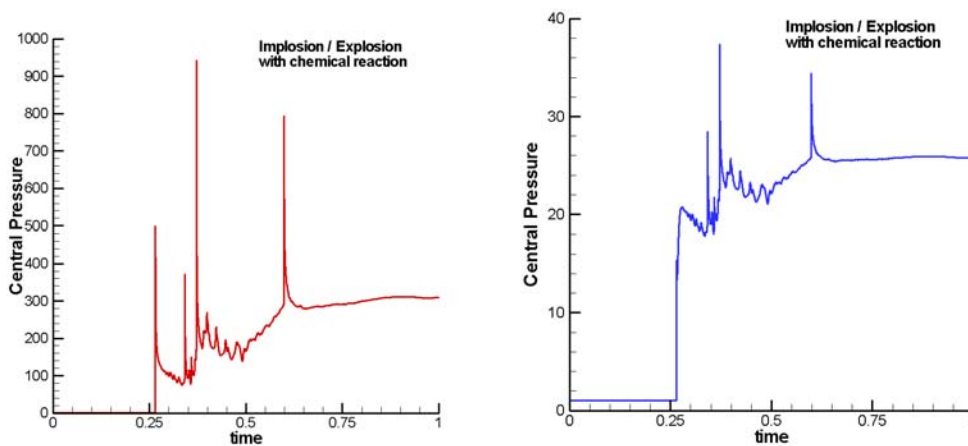


Figure 5.6 Time histories temperature and pressure and at the focal point for the imploding reacting flow.

VI. Concluding remarks

Direct numerical calculations of one- and two-dimensional implosion/explosion for efficient detonation initiation have been conducted. By using the space-time CESE method, we have obtained excellent interpretation of events that happen during the implosion/explosion processes. In one-dimensional calculations, we clearly showed a consecutive two-implosion system due to the interaction between the reflected main shock and the contact discontinuity. This double implosion shock system pushes the pressure and the temperature at the focal point to be more than 5000 times higher than its initial conditions. Thus it greatly facilitates the detonation initiation processes. In two-dimensional calculations, we focus on polygonal converging shocks. In the implosion phase, numerical images clearly showed the regenerations of rotated and smaller polygonal forms. Both the implosion and explosion flow patterns are complex and spectacular. Time histories of flow variables at the focal point confirm the double implosion mechanism found in the one-dimensional results. These results clearly demonstrate that the space-time CESE method is capable to catch all salient features of complex implosion/explosion flows.

VII. Acknowledgements

We are indebted to Professor J. E. Shepherd of Cal. Tech. for suggesting the general direction of this research work. Useful interactions with other members in the ONR PDE program are also acknowledged. Financially support by ONR, Grant No. N00014-04-1-0559, monitored by Dr. Gabriel Roy, is greatly appreciated.

VIII. References

1. Murray, S., Zhang, D., and Gerrard, K., "Critical Parameters for Pulse Detonation Engine Pre-detonator Tubes," International Colloquium on the Dynamics of Explosions and Reactive Systems, Hakone, Japan, July, 2003.
2. Jackson, S. I., Grunthaner, M., and Shepherd, J. E., "Wave implosion as an initiation mechanism for pulse detonation engines." 39th AIAA/ASME/SAE/ASEE Joint Propulsion Conference and Exhibit, July 20-23, 2003, Huntsville, AL, AIAA 2003-4820.
3. Jackson, S. I. and Shepherd, J. E., "Initiation Systems for Pulse Detonation Engines," 38th AIAA/ASME/SAE/ASEE Joint Propulsion Conference and Exhibit, July 7-10, 2002, Indianapolis, IN, AIAA 2002-3627.
4. Taylor, G. I., "The Formation of a Blast Wave by a Very Intense Explosion. I. Theoretical Discussion," Proc. Roy. Soc. A, Vol. 201, 1950, pp. 159-174.
5. Sedov, L. I., "Similarity and Dimensional Methods in Mechanics," Cleaver Hume, 1959 London, Chaps. 4,5.
6. Sharma, V. D. and Radha, C. H., "Similarity solutions for converging shocks in a relaxing gas", International Journal of Engineering Science, Vol. 33, No. 4, 1995, pp. 535-553.
7. Toque, N., "Self-similar implosion of a continuous stratified medium", Shock Waves, Vol. 11, 2001, pp. 157-165.
8. Van Dyke, M., and Guttman, A., "The converging shock wave from a spherical or cylindrical piston". J. Fluid Mech., Vol. 120, 1982, pp. 451-462.
9. Guderley, G., "Kugelige and Zylindrische Verdichtungsstosse in der Nake des Kugelmittelpunktes Lzw der Zylinderachse". Luftfahrtforschung, Vol. 19, 1942, pp. 302-312.
10. Boyer, D.W., "An experimental study of the explosion generated by a pressurized sphere", J. Fluid Mech., Vol. 9, 1960, pp. 401-429.
11. Friedman, M.P., "A simplified analysis of spherical and cylindrical blast waves", J. Fluid Mech., Vol. 11, 1961, pp. 1-15.
12. Glass, I. I., "Non-stationary Flows and Shock Waves," Oxford Science Publications, Oxford, 1994, Chap. 12.
13. Baker, W.E., Explosions in Air, Wilfred Baker Engineering, San Antonio, 1973, Chap. 7.
14. Schwendeman, D. W. and Whitham, G. B., "On converging shock waves," Proc. R. Soc. Lond. A., Vol.413, 1987, pp. 297-311.
15. Flores, J. and Holt, M., "Grimm's method applied to underwater explosions", J. Comp. Phys., Vol. 44, 1981, pp. 377-387.

16. Charrier, P. and Tessieras, B., "A front-tracking method applied to hyperbolic systems of nonlinear conservation Laws", *SIAM J. Numer. Anal.*, Vol. 23, 1986, pp. 461–472.
17. Oran, E. S. and DeVore, C. R., "The stability of imploding detonations: results of numerical simulations," *Phys. Fluids*, Vol. 6(1), 1996, pp. 369-380.
18. Payne, R. B., "A numerical method for a converging cylindrical shock," *J. Fluid Mech.*, Vol. 2, 1956, pp. 285-200.
19. Falcovitz, J. and Birman, A., "A singularities tracking conservation laws scheme for compressible duct flows", *J. Comp. Phys.*, 115, 1994, pp. 431–439.
20. Cook Jr., G., "High accuracy capture of curved shock fronts using the method of space-time conservation element and solution element," 37th AIAA Aerospace Sciences Meeting and Exhibit, Reno, NV, January 11-14, 1999.
21. Chang, S.C., "The method of space-time conservation element and solution element – a new approach for solving the Navier Stokes and Euler equations," *J. Comput. Phys.*, Vol. 119, 1995, pp. 295-324.
22. Chang, S.C., Wang, X.Y. and Chow, C.Y., "The space-time conservation element and solution element method: a new high-resolution and genuinely multidimensional paradigm for solving conservation laws", *J. Comp. Phys.*, Vol. 156, 1999, pp. 89-136.
23. Chang, S. C., Wang, X. Y. and To, W. M., "Application of the space-time conservation element and solution element method to one- dimensional convection-diffusion problems," *J. Comput. Phys.*, Vol. 165, 2000, pp. 189-215.
24. Zhang, Z.C., Yu, John S. T., and Chang, S.C., "A space-time conservation element and solution element method for solving the two- and three-dimensional unsteady Euler equations using quadrilateral and hexahedral meshes", *J. Comput. Phys.*, Vol. 175, 2002, pp. 168-199.
25. Eckett, C. A., Quirk, J. J., and Shepherd, J. E., "The Role of Unsteadiness in Direct Initiation of Gaseous Detonations," *J. Fluid Mech.* 421, 2000, pp. 147-183.
26. Yu, S. T., Chang, S. C., and Jorgenson, P. C. E., "Direct Calculation of Detonation with Multi-Step Finite-Rate Chemistry by the Space-Time Conservation Element and Solution Element Method," AIAA Paper 99-3772, AIAA 30th Fluid Dynamics Conference and Exhibit, June 1999, Norfolk, VA.
27. Im, K.-S., Kim, C.-K., and Yu, S.-T. J., "Application of the CESE Method to Detonation with Realistic Finite-Rate Chemistry," AIAA-2002-1020 the 40th Aerospace Sciences Meeting and Exhibit, January 2002, Reno, NV.
28. Yu, S.T. and Chang, S.C., "Treatments of Stiff Source Terms in Conservation Laws by the Method of Space-Time Conservation Element and Solution Element," AIAA Paper 97-0435, 35th AIAA Aerospace Sciences Meeting, January 1997, Reno, NV.
29. Yu, S.T. and Chang, S.C., "Applications of the Space-Time Conservation Element and Solution Element Method to Unsteady Chemically Reactive Flows," AIAA Paper 97-2007, in A Collection of Technical papers, 13th AIAA CFD Conference, June 1997, Snowmass, CO.
30. Toro, E. F., "Riemann Solvers and Numerical Methods for Fluid Dynamics," 2nd, Springer, 1999 London, pp.582-585.